Measuring linear and non-linear galaxy bias using counts-in-cells in the Dark Energy Survey Science Verification data

A. I. Salvador,[1] F. J. Sánchez [ID],[2,3]★ A. Pagul,[4,5] J. García-Bellido,[1] E. Sanchez,[3]
A. Pujol [ID],[6,7] J. Frieman,[5,8] E. Gaztanaga,[9,10] A. J. Ross,[11] I. Sevilla-Noarbe,[3]
T. M. C. Abbott,[12] S. Allam,[8] J. Annis,[8] S. Avila,[13] E. Bertin,[14,15] D. Brooks,[16]
D. L. Burke,[17,18] A. Carnero Rosell,[19,20] M. Carrasco Kind,[21,22] J. Carretero,[23]
F. J. Castander,[9,10] C. E. Cunha,[17] J. De Vicente,[3] H. T. Diehl,[8] P. Doel,[16]
A. E. Evrard,[24,25] P. Fosalba,[9,10] D. Gruen,[17,18] R. A. Gruendl,[21,22] J. Gschwend,[19,20]
G. Gutierrez,[8] W. G. Hartley,[16,26] D. L. Hollowood,[27] D. J. James,[28] K. Kuehn,[29]
N. Kuropatkin,[8] O. Lahav,[16] M. Lima,[19,30] M. March,[31] J. L. Marshall,[32]
F. Menanteau,[21,22] R. Miquel,[23,33] A. K. Romer,[34] A. Roodman,[17,18] V. Scarpine,[8]
R. Schindler,[18] M. Smith,[35] M. Soares-Santos,[36] F. Sobreira,[19,37] E. Suchyta,[38]
M. E. C. Swanson,[22] G. Tarle,[25] D. Thomas,[13] V. Vikram,[39] and A. R. Walker[12]
(DES Collaboration)

Affiliations are listed at the end of the paper

ABSTRACT

Non-linear bias measurements require a great level of control of potential systematic effects in galaxy redshift surveys. Our goal is to demonstrate the viability of using counts-in-cells (CiC), a statistical measure of the galaxy distribution, as a competitive method to determine linear and higher-order galaxy bias and assess clustering systematics. We measure the galaxy bias by comparing the first four moments of the galaxy density distribution with those of the dark matter distribution. We use data from the MICE simulation to evaluate the performance of this method, and subsequently perform measurements on the public Science Verification data from the Dark Energy Survey. We find that the linear bias obtained with CiC is consistent with measurements of the bias performed using galaxy–galaxy clustering, galaxy–galaxy lensing, cosmic microwave background lensing, and shear + clustering measurements. Furthermore, we compute the projected (2D) non-linear bias using the expansion $\delta_g = \sum_{k=0}^{3}(b_k/k!)\delta^k$, finding a non-zero value for b_2 at the 3σ level. We also check a non-local bias model and show that the linear bias measurements are robust to the addition of new parameters. We compare our 2D results to the 3D prediction and find compatibility in the large-scale regime ($>30\,h^{-1}\,\mathrm{Mpc}$).

Key words: cosmological parameters – cosmology: observations – dark energy – large-scale structure of Universe.

1 INTRODUCTION

In recent years, photometric redshift galaxy surveys, such as the Sloan Digital Sky Survey (Kollmeier, Zasowski & Rix 2017), the

Dark Energy Survey (DES) (Dark Energy Survey Collaboration 2016), and the future Large Synoptic Survey Telescope (Ivezić et al. 2008) and Euclid (Amiaux, Scaramella & Mellier 2012), have arisen as powerful probes of the large-scale structure (LSS) of the Universe and of dark energy. The main advantage of these surveys is their ability to retrieve information from a vast number of objects, yielding unprecedented statistics for different observables in the study of

★ E-mail: francs1@uci.edu

LSS. Their biggest drawback is the lack of line-of-sight precision and the systematic effects associated with it. Thus, well-constrained systematic effects and robust observables are required in order to maximize the performance of such surveys. In this context, simple observables such as the galaxy number counts serve an important role in proving the robustness of a survey. In particular, the galaxy counts-in-cells (CiC), a method that consists of counting the number of galaxies in a given 3D or angular aperture, has been shown to provide valuable information about the LSS (Peebles 1980; Efstathiou et al. 1990; Bernardeau 1994; Gaztañaga 1994; Szapudi 1998) and gives an estimate of how different systematic effects can affect measurements. The CiC can provide insights to higher-order statistical moments of galaxy counts without requiring the computation resources of other methods (Gil-Marín et al. 2015), such as the three- or four-point correlation functions.

Understanding the relation between galaxies and matter (galaxy bias) is essential for the measurement of cosmological parameters (Gaztañaga et al. 2012). The uncertainties in this relation strongly increase the errors in the dark energy equation of state or gravitational growth index (Eriksen & Gaztanaga 2015). Thus, having a wide variety of complementary methods to determine galaxy biasing can help break degeneracies and improve the overall sensitivity for a given galaxy survey.

In this paper we present a method to extract information from the galaxy CiC. Using this method, we measure the projected (angular) galaxy bias (linear and non-linear) in both simulations and observational data from DES, we compare the measured and predicted linear and non-linear bias, and we test for the presence of systematic effects. This data set is ideal for this study since it has been already used for CiC in Clerkin et al. (2017), where it was found that the galaxy density distribution and the weak lensing convergence (κ_{WL}) are well described by a lognormal distribution. The main difference between our study and that of Clerkin et al. (2017) is that our main goal is to provide a measurement of the galaxy bias, whereas Clerkin et al. (2017) study convergence maps.

Gruen et al. (2017) also perform CiC in DES data. Combining gravitational lensing information and CiC, they measure the galaxy density probability distribution function (PDF) and obtain cosmological constraints using the `redMaGiC`-selected galaxies (Rozo et al. 2016) in DES Y1A1 photometric data (Drlica-Wagner et al. 2018). In our case we measure the moments of the galaxy density contrast PDF and compare them to the matter density contrast PDF from simulations (with the same redshift distributions) to study different biasing models, in a different galaxy sample (DES SV).

Throughout the paper, we assume a fiducial flat lambda cold dark matter (ΛCDM) $+ \nu$ (one massive neutrino) cosmological model based on Planck 2013 + *WMAP* polarization + ACT/SPT + BAO, with the parameters (Ade et al. 2014) $\omega_b = 0.0222$, $\omega_c = 0.119$, $\omega_\nu = 0.00064$, $h = 0.678$, $\tau = 0.0952$, $n_s = 0.961$, and $A_s = 2.21 \times 10^{-9}$ at a pivot scale $\bar{k} = 0.05\,\mathrm{Mpc}^{-1}$ (yielding $\sigma_8 = 0.829$ at $z = 0$), where $h \equiv H_0/100\,\mathrm{km\,s^{-1}\,Mpc^{-1}}$ and $\omega_i \equiv \Omega_i\,h^2$ for each species i.

The paper is organized as follows: In Section 2 we present the data sample used for our analysis. First, we present the simulations used to test and validate the method and afterwards, the data set in which we perform our measurements. In Section 3 we present the CiC theoretical framework and detail our method to obtain the linear and non-linear bias. Sections 4 and 5 present the CiC moments and bias calculations for the MICE simulation and DES SV data set, respectively. In Section 6 we study the systematic uncertainties in our method. Finally, in Section 7, we include some concluding remarks about this work.
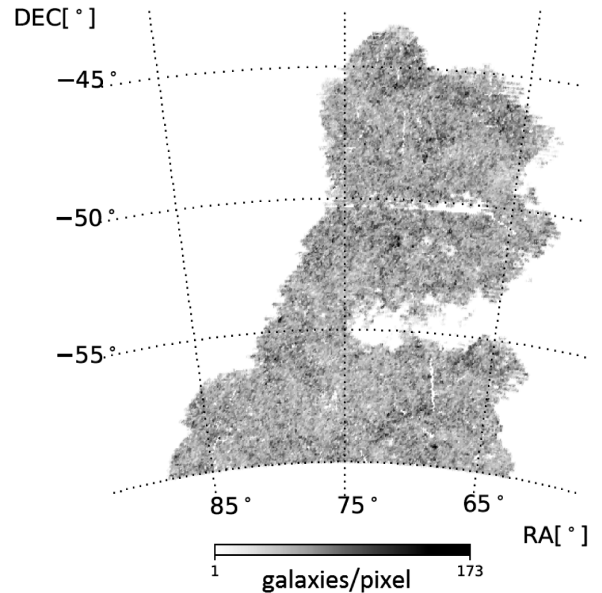
Figure 1. Footprint of the DES SV benchmark sample (Crocce et al. 2016). We use approximately 2.3 million objects contained within this area for our studies.

2 DATA SAMPLE

2.1 Simulations

In order to test and validate the methodology presented in this paper, we use the MICE simulation (Fosalba et al. 2008; Crocce et al. 2010). MICE is an *N*-body simulation with cosmological parameters following a flat ΛCDM model with $\Omega_{\mathrm{m}} = 0.25$, $\Omega_\Lambda = 0.75$, $\Omega_{\mathrm{b}} = 0.044$, $n_s = 0.95$, and $\sigma_8 = 0.8$. The simulation covers an octant of the sky, with redshift z between 0 and 1.4, and contains 55 million galaxies in the light-cone. The simulation has a comoving size $L_{\mathrm{box}} = 3072\,h^{-1}$ Mpc and more than 8×10^9 particles (Crocce et al. 2015). The galaxies in the MICE simulation are selected following the procedure in Crocce et al. (2016), imposing the threshold $i_{\mathrm{evol}} < 22.5$. The MICE simulation has been extensively studied in the literature (Sánchez et al. 2011; Hoffmann, Bel & Gaztanaga 2015; Crocce et al. 2016; Pujol et al. 2017; Garcia-Fernandez et al. 2018), including measurements of the higher-order moments in the dark matter field (Fosalba et al. 2008), providing an ideal validation sample.

2.2 The DES SV benchmark data sample

In this paper we perform measurements of the density contrast distribution and its moments on the DES Science Verification (SV) photometric sample[1] (Fig. 1). The DES SV observations were taken using DECam on the Blanco 4 m telescope near La Serena, Chile, covering over 250 deg^2 at close to the DES nominal depth. From this sample we make selection cuts in order to recover the LSS benchmark sample (Crocce et al. 2016). By doing this we minimize the possible two-point systematic effects and we ensure completeness. We focus on the SPT-E field, since it is the largest contiguous field and the best analysed, with $60° < \mathrm{RA} < 95°$ and $-60° < \mathrm{Dec.} < -40°$ considering only objects with $18 < i < 22.5$, where i is MAG_AUTO as measured by SExtractor (Bertin & Arnouts

---

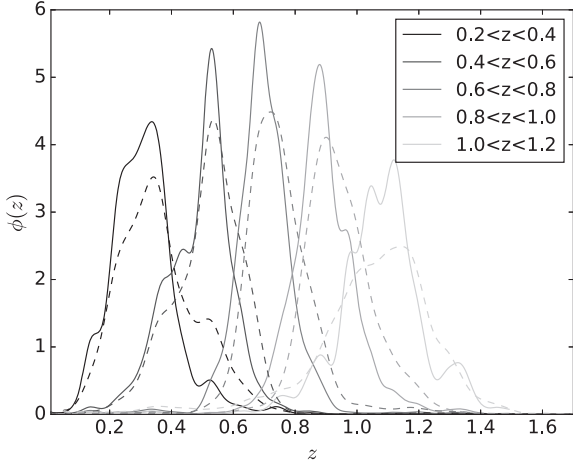[1]This sample is available at https://des.ncsa.illinois.edu/releases/sva1.

Figure 2. Redshift distribution of the galaxies in each photometric redshift bin using TPZ (solid line) and BPZ (dashed line) in DES SV benchmark data from Crocce et al. (2016). These distributions have been obtained by stacking the photometric redshift PDFs of galaxies in a spectroscopic subsample detailed in Sánchez et al. (2014). Lighter lines represent higher redshift slices.

1996) in the *i* band. The star–galaxy separation is performed by selecting objects such that WAVG_SPREAD_MODEL > 0.003. The total area considered for our study is then 116.2 deg^2 with approximately 2.3 million objects and a number density $n_g = 5.6$ arcmin^{-2}. Several photo-*z* estimates are available for these data (Sánchez et al. 2014). We will focus on the TPZ (Carrasco Kind & Brunner 2013) and BPZ (Benitez 2000) catalogues. We use the same five redshift bins used in Crocce et al. (2016). We use the redshift distributions from Sánchez et al. (2014), which are depicted in Fig. 2. These distributions have been obtained by comparing the DES SV photometric sample including spectroscopic data from zCOSMOS (Lilly et al. 2007, 2009) and VVDS Deep (Le Fèvre et al. 2013) among other data sets. For more details about the photometric redshift measurement and calibration, we refer the reader to Sánchez et al. (2014).

Several measurements of the linear bias have been performed using this field (Crocce et al. 2016; Giannantonio et al. 2016; Prat et al. 2018), making it ideal for this study.

3 THEORETICAL FRAMEWORK AND METHODOLOGY

3.1 Counts-in-cells

Counts-in-cells (Peebles 1980) is a method used to analyse the LSS based on dividing a galaxy survey into cells of equal volume (V_{pix}) and counting the number of galaxies in each cell, (N_{gal}). This method has also been extensively used in the literature to characterize the galaxy distribution (Efstathiou et al. 1990; Bernardeau 1994; Gaztañaga 1994; Szapudi 1998) and, recently, even the neutral hydrogen in simulations (Leicht et al. 2018). In the case of photometric redshift surveys, the lack of precision in the redshift determination makes angular aperture cells more appealing. Numerous examples of the application of CiC using angular aperture cells can be found in the literature (Gaztañaga 1994; Szapudi et al. 2002; Ross, Brunner & Myers 2006; Yang & Saslaw 2011; Wolk et al. 2013).

It is particularly useful to work with the density contrast δ_i in each cell (or pixel), *i*, defined as

$$\delta_i \equiv \frac{\rho_i}{\langle\rho\rangle} - 1, \tag{1}$$

where $\rho_i \equiv \frac{N_{i,gal}}{A_{i,pix}}$ is the galaxy density in the pixel of area $A_{i,pix}$ and $\langle\rho\rangle$ is the mean density. In this work, we are going to use $\langle\rangle$ to denote statistical averages. Given these definitions, it follows that $\langle\delta\rangle = 0$.

In order to study the statistical properties of the density contrast distribution, δ, we are interested in the measurement of the average of the *J*-point correlation functions, $\overline{w}_J(\theta)$, in a cell of solid angle $A = 2\pi(1 - \cos\theta)$ (Gaztañaga 1994):

$$\overline{w}_J(\theta) = \frac{1}{A^J} \int_A dA_1...dA_J w_J(\theta_1, ..., \theta_J), \ J \geq 2, \tag{2}$$

with $dA_i = \sin\theta_i d\theta_i d\phi_i$ and $w_J(\theta)$ the *J*-point angular correlation function.

To estimate the angle-averaged *J*-point correlation function, $\overline{w}_J(\theta)$, we use the corrected connected moments, $\langle\delta^J\rangle_c$, taking into account the discrete nature of CiC and assuming Poisson-like shot-noise contributions as introduced by Gaztañaga (1994). In particular, we are interested in terms up to $J = 4$:

$$\overline{w}_2(\theta) = \langle\delta^2\rangle_c = \langle\delta^2\rangle - \frac{1}{\overline{N}},$$

$$\overline{w}_3(\theta) = \langle\delta^3\rangle_c = \langle\delta^3\rangle - \frac{3}{\overline{N}}\langle\delta^2\rangle_c - \frac{1}{\overline{N}^2},$$

$$\overline{w}_4(\theta) = \langle\delta^4\rangle_c = \langle\delta^4\rangle - 3\langle\delta^2\rangle^2 - \frac{7}{\overline{N}^2}\langle\delta^2\rangle_c - \frac{6}{\overline{N}}\langle\delta^3\rangle_c - \frac{1}{\overline{N}^3}, \tag{3}$$

where $\overline{N} = \frac{N_{gal}^{tot} * A_{pix}}{A_{tot}}$ and N_{gal}^{tot} is the total number of galaxies, A_{tot} is the total area, and A_{pix} is the area of the pixel.

For our study we use the rescaled connected moments S_J, defined as

$$S_J \equiv \frac{\overline{w}_J(\theta)}{[\overline{w}_2(\theta)]^{J-1}}, \ J > 2, \tag{4}$$

$$S_2 = \overline{w}_2(\theta). \tag{5}$$

In most previous studies, the cells considered were spheres with radii of varying apertures (Peebles 1980; Bernardeau 1994). We perform our measurements of the projected (angular) density contrast by dividing the celestial sphere into HEALPix pixels (Górski et al. 2005). For our study we vary the HEALPix parameter N_{side} from 32 to 4096 (i.e. apertures ranging from 1.83° to 0.014°). The angular aperture, θ, is estimated as the square root of the pixel area. According to equation (2) there is a dependence on the boundaries of the cell and thus on the shape that we choose for the pixels. Gaztañaga (1994) estimates CiC for square cells of side *l* in a range $l = 0.03°–20°$ and compares to the average correlation functions $\overline{w}_2(\theta)$. The agreement between the two estimates indicates that square cells give very similar results to circular cells when the sizes of the cells are scaled to $\theta = l/\sqrt{\pi}$. Using data from MICE, we perform several tests to see that the concrete shape of the pixel, when it is close to a regular polygon, does not affect the measured moments despite boundary effects (Appendix A). Furthermore, when working with the acquired observational data, the geometry of the survey becomes complicated. A discussion of how we deal with this is found in Appendix B. The error bars throughout this paper are estimated using the bootstrap method (Efron 1979; Masci &
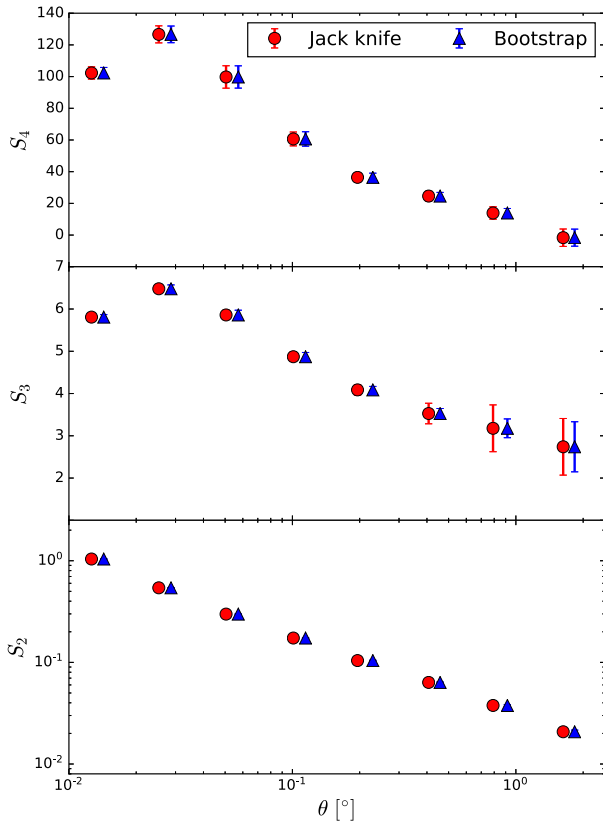
Figure 3. Moments of the density contrast distribution as a function of cell scale in the MICE simulation for the redshift bin $0.2 < z < 0.4$, with jack-knife errors (solid circles) and bootstrap errors (solid triangles). The results for a given scale θ have been separated in the figure for visualization purposes, being the blue triangles, the ones shown at the nominal measured scale.

SWIRE Team 2006; Ivezić et al. 2014). This choice is mainly due to the lack of number of samples for large pixel sizes that might limit the precision of other methods such as the jack-knife, given that the latter depends highly on the number of samples, as pointed out in Norberg et al. (2009). Fig. 3 shows agreement between the uncertainties computed using the jack-knife and bootstrap methods for a randomly chosen redshift bin in the MICE simulation. We use $N_b = \min(N_{pix}, 100)$ bootstrap and jack-knife realizations of the density contrast distribution to estimate our errors, where N_{pix} is the total number of unmasked pixels in our map.

3.2 Galaxy bias

One of the most important applications of the CiC observable is the determination of the galaxy bias. We observe the galaxy distribution and use it as a proxy to the underlying matter distribution. Both baryons and dark matter structures grow around primordial overdensities via gravitational interaction, so these distributions should be highly correlated. This relationship is called the *galaxy bias*, which measures how well galaxies trace the dark matter. Galaxy biasing was seen for the first time analysing the clustering of different populations of galaxies (Davis, Geller & Huchra 1978; Dressler 1980). The theoretical relation between galaxy and mass distributions was suggested by Kaiser (1984) and developed by Bardeen et al. (1986). Since then, many different prescriptions have arisen

(Fry & Gaztañaga 1993; Bernardeau 1996; Mo & White 1996; Sheth & Tormen 1999; Manera, Sheth & Scoccimarro 2010; Manera & Gaztañaga 2011). However, there is no generally accepted framework for galaxy biasing. While the galaxy and dark matter distribution are related, the exact relation depends on galaxy formation (Press & Schechter 1974), galaxy evolution (Nusser & Davis 1994; Tegmark & Peebles 1998; Blanton et al. 2000), and selection effects. Bias depends strongly on the environment. Using dark matter simulations, Pujol et al. (2017) show how the halo bias is determined by local density and not by halo mass. Several studies have demonstrated the different behaviours of early-type and late-type galaxies at both small and large scales (Willmer et al. 1999; Norberg et al. 2002; Zehavi et al. 2002; Ross et al. 2006). To have a good estimate of the real matter distribution, it is convenient to use a galaxy sample that is as homogeneous as possible. With the linear bias $b(z)$ approximation, we can relate the matter fluctuations δ_m with the fluctuations in the galaxy distribution δ_g:

$$\delta_g = b\delta_m. \tag{6}$$

In the linear approximation, up to scalings, all statistical properties are preserved by the biasing and the observed galaxy properties reflect the matter distribution on large scales, as long as we consider only two-point statistics. However, in the general case, it is highly unlikely that the relation is both local and linear. Non-local dependencies might come from some properties such as the local velocity field or derivatives of the local gravitational potential (Fry & Gaztañaga 1993; Scherrer & Weinberg 1998). Bias also depends on redshift (Fry 1996; Tegmark & Peebles 1998). When non-Gaussianities are taken into account, linear bias fails to be a good description. If we want to measure higher orders, we can assume that the (smoothed) galaxy density can be written as a function of the mass density and expand it as a Taylor series (assuming a local relation) (Frieman & Gaztañaga 1999; Fry & Gaztañaga 1993):

$$\delta_g = f(\delta) = \sum_{k=0}^{\infty} \frac{b_k}{k!} \delta_m^k. \tag{7}$$

The linear term $b_1 = b$ is the usual linear bias. Using this expansion we can relate the dark matter and the galaxy density contrast moments using the following relationships (Fry & Gaztañaga 1993):

$$S_{2,mod} = b^2 S_{2m}, \tag{8}$$

$$S_{3,mod} = b^{-1}(S_{3m} + 3c_2), \tag{9}$$

$$S_{4,mod} = b^{-2}\left(S_{4m} + 12c_2 S_{3m} + 4c_3 + 12c_2^2\right), \tag{10}$$

where $c_k = b_k/b$ for $k \geq 2$, the subscript 'm' refers to the underlying matter distribution and the subscript 'mod' to the galaxy distribution. We will refer to this model as local.

Bel, Hoffmann & Gaztañaga (2015) point out that ignoring the contribution from the non-local bias can affect the linear and non-linear bias results. As a consequence, we analyse the case when the non-local contribution is included. To do so, we substitute c_2 by $c_2' = c_2 - \frac{2}{3}\gamma_2$, where γ_2 is the so-called non-local bias parameter (Bel et al. 2015). We will refer to this model as non-local.

Note that we omit the terms higher than third order because, as we will show later, we have very limited sensitivity to b_3, and expect to have no sensitivity to b_4.
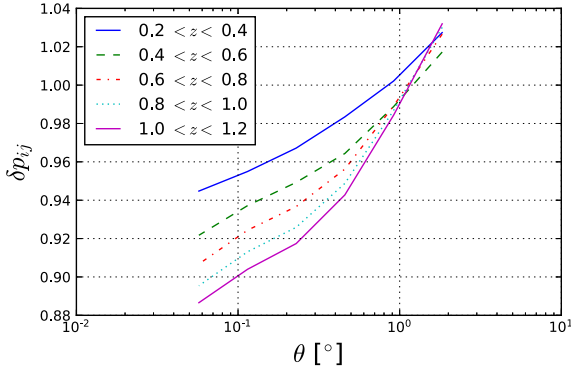
Figure 4. Ratio between $S_{2,\mathrm{m}}$ for $\Omega_\mathrm{m} = 0.2$ (the minimum allowed by Planck priors) and $S_{2,\mathrm{m}}$ for our fiducial model as a function of the cell aperture angle θ. The different lines represent different redshift bins. We see that the variation is within 12 per cent of the linear prediction.

3.3 Estimating the projected linear and non-linear bias

The relations in equations (8–10) refer to the 3D case and connect an observed galaxy distribution with its underlying dark matter distribution, both tracing the same redshift range and cosmological parameters. We assume that this bias model is also valid for the projected moments (we will check the validity of this assumption later). Moreover, given the measurements in a dark matter simulation with the same redshift distribution and angular footprint as our galaxy data set, we estimate the linear and non-linear bias of these galaxies using equations (8–10). Note that these relations apply when we are comparing two data sets with the same value for the σ_8 parameter. In the case that $\sigma_8 \neq \sigma_{8,\mathrm{m}}$ we will have to correct the resulting bias so

$$b_\mathrm{corr} = b_\mathrm{uncorr} \frac{\sigma_{8,\mathrm{m}}}{\sigma_8}. \tag{11}$$

We will use this correction in Section 6.3. We also take advantage of the fact that the skewness and kurtosis depend weakly on the cosmological parameters (Bouchet et al. 1992). In particular, a 5 per cent variation choosing $\Omega_\mathrm{m} = 0.25$ translates to a variation of 0.2 per cent in the measured $S_{3\mathrm{m}}$, which is much smaller than the statistical fluctuations that we expect from our samples. In the case of $S_{4\mathrm{m}}$ our sensitivity is even lower, making it safe to use a simulation with the same footprint and redshift distribution, as long as the variation in the cosmological parameters is small. However, this is not necessarily true for the case of $S_{2\mathrm{m}}$, where the dependency on the cosmological parameters is higher. We check this using equation (2) to compute the projected $S_{2\mathrm{m}}$ for two different sets of cosmological parameters: our fiducial Planck cosmology (Ade et al. 2014) and a model with $\Omega_\mathrm{m} = 0.2$. We use a Gaussian selection function $\phi(z)$ with $\sigma_z = 0.05(1 + z)$ since this is representative of the data sets that we analyse in this work. After this, we check the ratio

$$\delta p_{ij}(z, \theta) = \frac{S_{2\mathrm{m},i}(z, \theta)}{S_{2\mathrm{m},j}(z, \theta)} \frac{D_{+,j}^2(\bar{z})}{D_{+,i}^2(\bar{z})} \tag{12}$$

for the different redshift slices considered in our analysis, where the subscripts i and j correspond to two different sets of cosmological parameters and $D_+(\bar{z})$ is the linear growth factor (Heath 1977; Peebles 1980) evaluated at the mean redshift of the considered slice. This gives us an upper limit to the expected variation in $S_{2\mathrm{m}}$ to consider in our analysis. In Fig. 4 we can see that the variation is within 12 per cent of the linear prediction; thus, we conservatively assign 12 per cent systematic error to $S_{2\mathrm{m}}$ due to this variation.

Under these conditions we perform a simultaneous fit to b, b_2, b_3, and γ_2. In order to do so we consider the likelihood:

$$\log \mathcal{L} = -\frac{1}{2} \sum_{k=2}^{4} \sum_{i,j} \left[S_{k,\mathrm{g}}(\theta_i) - S_{k,\mathrm{mod}}(\theta_i) \right]$$

$$\times C_{k,ij}^{-1} \left[S_{k,\mathrm{g}}(\theta_j) - S_{k,\mathrm{mod}}(\theta_j) \right] = -\frac{\chi^2}{2}, \tag{13}$$

where $S_{k,\mathrm{g}}$ are the measured galaxy moments and $S_{k,\mathrm{mod}}$ are the models in equations (8), (9), and (10). We checked that the measured S_k follow a Gaussian distribution. The covariances $C_{k,ij}$ are computed as follows:

$$C_{k,ij} = \frac{N_{u,\mathrm{pix}}(\theta_i)}{N_{u,\mathrm{pix}}(\theta_j)} 2^{2(j-i)} \sigma_k(\theta_i) \sigma_k(\theta_j), \tag{14}$$

with $N_{u,\mathrm{pix}}(\theta_i)$ being the number of pixels used in an aperture, θ_i. Note that, since we are using HEALPix, which imposes a fixed grid, and we are not repeating the measurements in translated/rotated galaxy fields, we are reusing the same galaxies for different scales, so the factor $\frac{N_{u,\mathrm{pix}}(\theta_i)}{N_{u,\mathrm{pix}}(\theta_j)} 2^{2(j-i)}$ accounts for the induced correlation due to this reuse. We assume that the errors in the dark matter moments and the errors in the galaxy moments are not correlated and add them in quadrature, so

$$\sigma_k(\theta_i) = \sqrt{\sigma_{k,\mathrm{g}}^2(\theta_i) + \sigma_{k,\mathrm{m}}^2(\theta_i)}, \tag{15}$$

where $\sigma_{k,\mathrm{g/m}}(\theta_i)$ is the standard deviation of the k-th (galaxy or matter) moment in an aperture θ_i computed using bootstrapping.

We use the following flat priors:

(i) $0 < b < 10$.
(ii) $-10 < b_2 < 10$.
(iii) $-10 < b_3 < 10$.
(iv) $\gamma_2 = 0$ (or in the case of the non-local model $-10 < \gamma_2 < 10$).

These priors have been chosen to prevent unphysical results. We evaluate the likelihood and obtain the best-fitting values and their uncertainties by performing a Markov chain Monte Carlo (MCMC) using the software package emcee (Foreman-Mackey et al. 2013). Summarizing, the method works as follows:

(i) Measure CiC moments using HEALPix pixels in the galaxy sample.
(ii) Measure CiC moments using the same pixels and selection function in a dark matter simulation with comparable cosmological parameters.
(iii) Evaluate the statistical and systematic uncertainties in the measured moments.
(iv) Obtain the best-fitting b, b_2, and b_3 (and γ_2 in the non-local model) using MCMC with the models from equations (8–10).

In summary, in the local model we fit three free parameters, whereas in the non-local model we fit four.

Hoffmann et al. (2015) present a prediction for the non-linear bias as a function of the linear bias in the 3D case:

$$b_2 = b^2 - 2.45b + 1.03, \tag{16}$$

$$b_3 = b^3 - 7.32b^2 + 10.79b - 3.90. \tag{17}$$

We will use these predictions to test the compatibility between the 3D and the measured projected values for the non-linear bias.
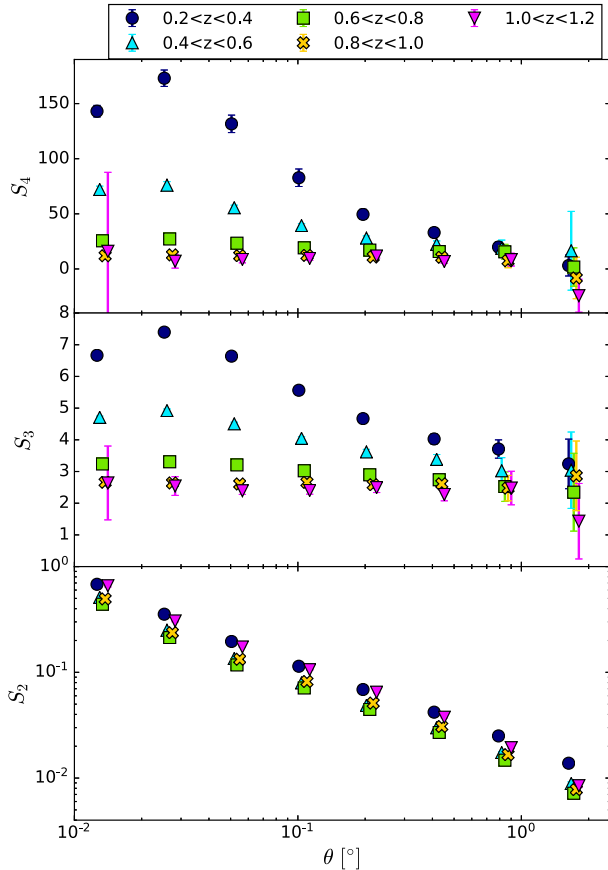
Figure 5. Moments of the density contrast distribution as a function of cell scale in the MICE simulation with Gaussian photometric redshift ($\Delta z = 0.2\sigma_z = 0.05(1 + z)$) for different redshift bins. The results for a given scale θ have been separated in the figure for visualization purposes.

4 RESULTS IN SIMULATIONS

In order to validate this method, we first compute the CiC moments in the MICE simulation (in both galaxies and DM) using a Gaussian selection function $\phi(z)$ with $\sigma_z = 0.05(1 + z)$. This σ_z is similar to the photometric redshifts found in the data using TPZ (Carrasco Kind & Brunner) and BPZ (Benitez 2000). We split our sample into five photometric redshift bins: $z \in [0.2, 0.4]$, $[0.4, 0.6]$, $[0.6, 0.8]$, $[0.8, 1.0]$, $[1.0, 1.2]$, mirroring the choice in Crocce et al. (2016). Then we do the same with the SV data sample presented in Section 2.2 with TPZ photometric redshifts.

4.1 Angular moments for MICE

Fig. 5 shows the moments of the density contrast distribution as a function of the cell scale for the different photometric redshift bins. We observe that the moments follow the expected trend; that is, lower redshift bins have higher values for the higher-order moments since non-linear gravitational collapse has a larger effect on these. This is true for all measurements except for the last two redshift bins of the variance S_2. This can be due to the magnitude cuts, since the galaxy populations are different at different redshifts. We also see that the larger the cell scale, the smaller the variance S_2, since larger cell scales should be more homogeneous. The skewness and kurtosis at linear scales ($\theta > 0.1°$) are constant and of the same order of magnitude as the expected values ($S_3 \approx 34/7$, S_4
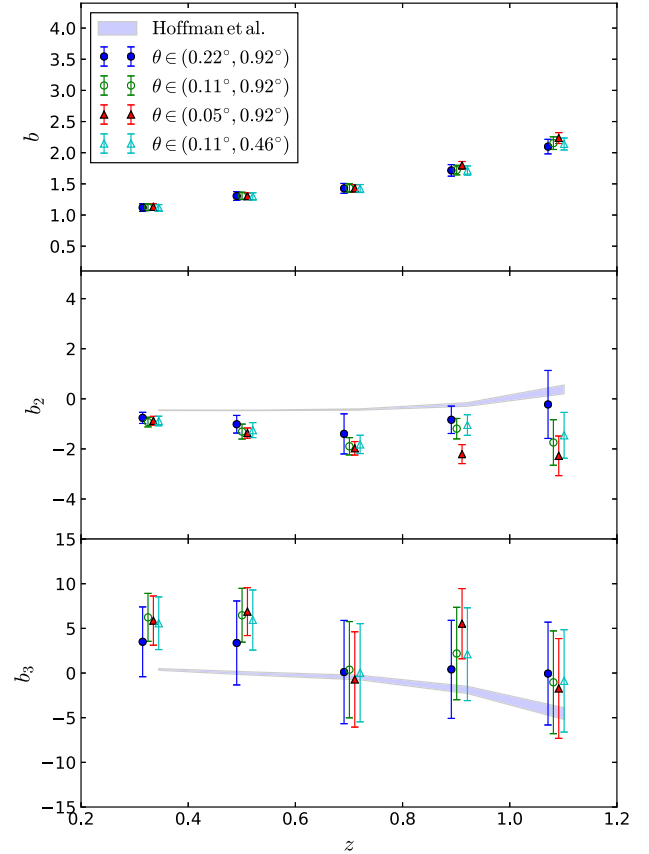
Figure 6. Linear and non-linear bias results as a function of redshift for MICE data with Gaussian photo-z. The different marker shapes represent the best-fitting results considering different ranges of the aperture angle θ. For the solid triangles we consider the range from $0.05°$ to $0.92°$, the open circles are our fiducial case with $0.11° < \theta < 0.92°$, for the solid circles, we take out the smallest scale in our fiducial case, and in the open triangles we take out the largest scale. The top panel shows the projected linear bias b as a function of redshift, the middle panel shows the best-fitting results for the projected b_2, and the lower panel shows b_3. The shaded region corresponds to the 3D predicted values using equation (17). The results for a given redshift z have been separated in the figure for visualization purposes.

$\approx 60\,712/1323$) (Bernardeau 1994). The behaviour at non-linear scales is due to the non-linearities of the MICE simulation.

4.2 Projected galaxy bias in MICE simulation

We smear the true redshift with the proper selection function in the MICE dark matter field, obtained from a dilution of the dark matter particles (taking 1/700 of the particles). Chang et al. (2016) demonstrate that the dilution of the dark matter field does not impact their statistics and using the measured moments from the previous section we proceed to perform a simultaneous fit for b, b_2, and b_3 using the local, non-linear bias model from equations (11)–(13). The fit results are summarized in Fig. 6. We can see the impact of changing the range of θ considered in the fit. In this case we see that including scales smaller than $0.1°$, where non-linear clustering has a large impact, affects the b_2 results. This, together with the fact that the reduced χ^2 minimum value doubles when including $\theta = 0.05°$, clearly shows that we should not consider scales smaller than $\theta = 0.1°$. We can see as well that b_3 is compatible with zero and that we have a limited sensitivity to it, given the area used. Thus, the

choice of ignoring terms of orders higher than b_3 becomes a good approximation. However, for b_2 we are able to measure a significant non-zero contribution. We can also see that the predicted values for the 3D non-linear bias parameter b_2 are not in good agreement at small scales, while there is an indication of better agreement at larger scales. This suggests that the 2D and 3D values for b_2 might be compatible at larger scales, in agreement with Manera & Gaztañaga (2011), who show that the local bias is consistent for scales larger than $R > 30$–$60 \, h^{-1}$ Mpc. They also show that the values of b_1 and b_2 vary with the scale and converge to a constant value around $R > 30$–$60 \, h^{-1}$ Mpc, which means that the values that we measure here have not yet fully converged. The prediction for b_3 seems to be compatible with the estimated values given the size of the error bars. These results show that we should consider b_2 as a first-order (small) correction to the linear bias model at these scales for projected (angular) measurements. The individual fits can be seen in Appendix C.

4.3 Verification and biasing model comparison

In order to verify this method and check if the local non-linear model considered induces certain systematic biases on the results, we check that the measured linear bias is compatible with corresponding measurements from the two-point correlation function (Fig. 7). In particular, we use the best-fitting parametrization from Crocce et al. (2016):

$$b_{\text{best}}(z) = 0.98 + 1.24z - 1.72z^2 + 1.28z^3. \tag{18}$$

In Fig. 7, we can see that the local bias and the non-local bias are in agreement, most likely due to the scale range that we are dealing with and the projection effects due to the size of the redshift slices. In this figure, we can also notice that the reduced chi-square for both models is similar, and that they are well below one. Given that the number of degrees of freedom is small, it is still possible that these values are correct; however, it is unlikely that this happens for all redshift bins. This suggests that, in agreement with Norberg et al. (2009), bootstrapping uncertainties are overestimated. However, we prefer to use these conservative uncertainties rather than state uncertainties that are too optimistic since one of the main goals of this work will be to state the statistical significance on the non-linear b_2 term. Another interesting feature in Fig. 7 is that the uncertainties in b_2 for the non-local model are considerably larger than those in the local model. This is due to the fact that γ_2 is highly correlated with b_2, which makes the posterior distribution for b_2 much wider, increasing the resulting uncertainty.

5 RESULTS IN DES SV DATA

5.1 Angular moments for DES SV

Using the same footprint, selection cuts, and redshift bins as in Crocce et al. (2016), we compute the moments of the density contrast distribution for the SV data. These results are depicted in Fig. 8 as a function of cell scale for different redshift bins. Here, as in the case of MICE, the variance decreases with the scale. The skewness and kurtosis are also constant and of the same order of magnitude as the theoretical values within errors. The largest differences when compared with the simulation are in the non-linear regime due to the different way in which non-linearities are induced in the simulation and in real data. We also compare to the results from Canada-France-Hawaii Telescope Legacy Survey (CFHTLS) found in Wolk et al. (2013). We find a similar general behaviour
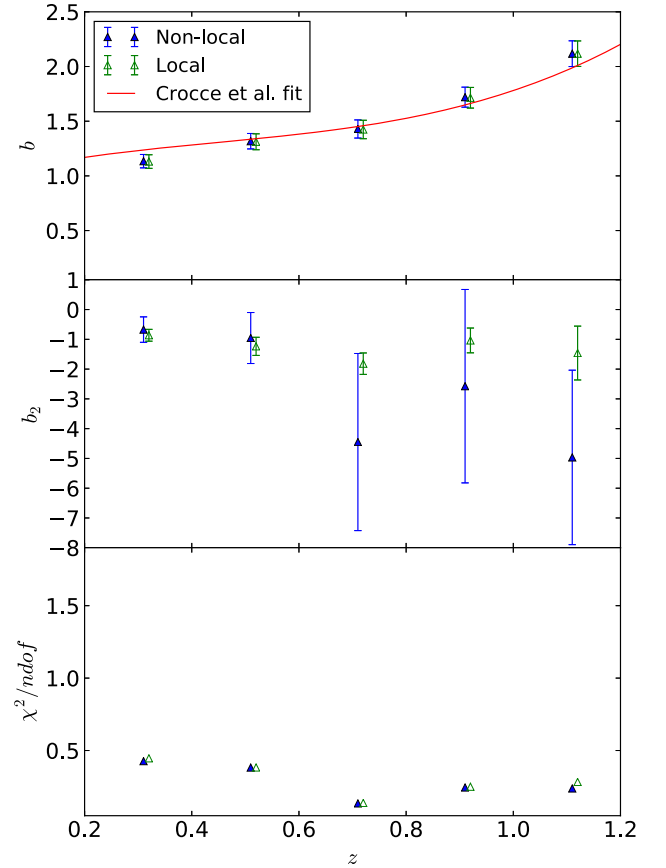

Figure 7. (Top) Comparison between the MICE simulation bias obtained using CiC with different biasing models: non-local (solid triangles) and local (open triangles). We also show the best fit from Crocce et al. (2016; figure 17) as reference. The middle panel shows the equivalent results for b_2. This is done for Gaussian photo-z with $\sigma_z = 0.05(1 + z)$. (Bottom) Total reduced chi-square for each of the models when fitting the moments to obtain the bias.

as well as the same order of magnitude in the measured S_3 and S_4. However, we do not expect the same exact results since the redshift distributions from CFHTLS do not match exactly the corresponding distributions in the DES SV data.

5.2 Projected galaxy bias in DES SV

Repeating the procedure that we used for the MICE galaxy simulation, we analyse the DES SV data and the MICE dark matter simulation, and compare their moments. In Fig. 9 we can see the results of simultaneously fitting for b, b_2, and b_3. The measurements in this figure include the systematic uncertainties that are introduced in Section 6. The resulting b is corrected by the ratio of σ_8 between MICE and our adopted fiducial cosmology using equation (11). The fit results can be seen in Appendix C. In this case, we detect a non-zero value for b_2. We check the probability of b_2 being zero by computing

$$\chi_z^2 = \sum_{i,j=1,N_{z\text{bins}}} \hat{b}_{2,i} \mathcal{C}_{2,ij}^{-1}(z) \hat{b}_{2,j}. \tag{19}$$

The sum runs for all the redshift bins. $\hat{b}_2$ is the weighted average of the fit results with the different fitting ranges and $\mathcal{C}_{2,ij}(z)$ is the covariance matrix for b_2. Taking into account the correlations
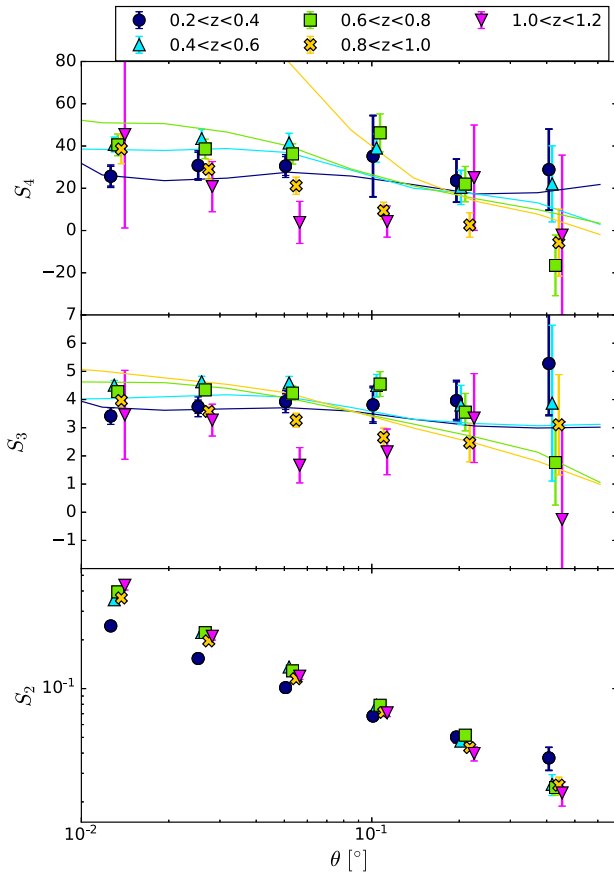
Figure 8. Moments of the density contrast distribution of the DES SV benchmark sample as a function of cell scale, for five different redshift bins and different scales. The results for a given scale θ have been separated in the figure for visualization purposes. We compare with the results from Wolk et al. (2013) for CFHTLS marked with solid lines of different colours for the different redshift bins: navy ($0.2 < z < 0.4$), cyan ($0.4 < z < 0.6$), lime ($0.6 < z < 0.8$), yellow ($0.8 < z < 1.0$).

between different redshift bins,

$$\mathcal{C}_{2,ij}(z) = \frac{N_{ij} N_{ji}}{N_{ii} N_{jj}} \Delta \hat{b}_{2,i} \Delta \hat{b}_{2,j}, \tag{20}$$

where N_{ij} is the number of galaxies observed in the photo-z bin i from the true-z bin j and $\Delta \hat{b}_{2,i}$ is the weighted uncertainty in $\hat{b}_{2,i}$ for the photo-z bin i. The value of $\chi_z^2 = 64.75$ with 4 degrees of freedom, so the probability is essentially 0, making it clear that the overall value of b_2 is non-zero for the local model. However, we lack the sensitivity necessary to detect a non-zero b_3.

We also check the measurement of linear bias obtained in this work and compare it with previous measurements on the same data set in Fig. 10. The measurements are generally in good agreement with each other, showing the robustness of the method.

Future DES data will have a considerably larger area and, as previous MICE measurements show, these measurements will improve. Here we also use the skewness and kurtosis of dark matter from the MICE dark matter simulation, as these quantities hardly depend on the cosmology (Bouchet et al. 1992). We also find that our results are similar to those in Ross et al. (2006). We do not expect them to be equal as the samples are different and the bias depends strongly on the population sample.
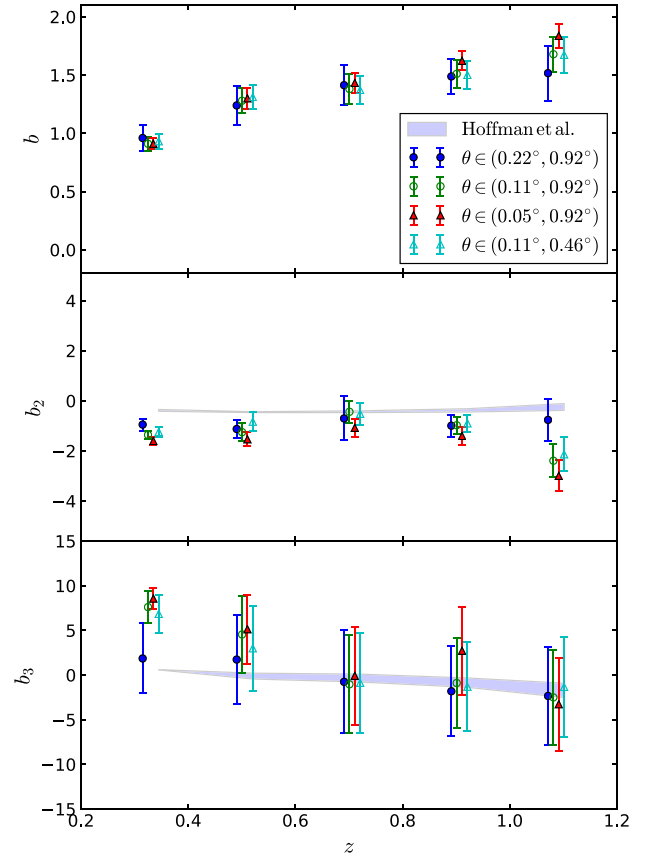
Figure 9. Linear and non-linear bias results as a function of redshift for DES SV data. Systematic uncertainties from Section 6 are already included in these results, excluding the uncertainties associated with the modelling. The different marker shapes represent the best-fitting results considering different ranges of aperture angle θ. For the solid triangles we consider the range from $0.05°$ to $0.92°$, open circles symbolize our fiducial case with $0.11° < \theta < 0.92°$, in solid circles, we take out the smallest scale in our fiducial case, and in open triangles we take out the largest scale. The shadowed region corresponds to the 3D predicted values using equation (17). The top panel shows the projected linear bias b as a function of redshift, the middle panel shows the best-fitting results for the projected b_2, the lower panel shows b_3. The results for a given redshift z have been separated in the figure for visualization purposes.

6 SYSTEMATIC ERRORS

In this section, we explore the effects that several potential sources of systematic uncertainty have on our moment measurements. Since our main observable is related to the number of galaxy counts in a given redshift interval, we are interested in observational effects that can affect this number. The main potential sources of systematic uncertainties are changes in airmass, seeing, sky brightness, star–galaxy separation, galactic extinction, and possible errors in the determination of the photometric redshift. In order to evaluate their effects, we use the maps introduced in Leistedt et al. (2016). To account for the stellar abundance in our field we proceed as in Crocce et al. (2016) and use the USNO-B1 catalogue (Monet et al. 2003). We also use the dust maps from Schlegel, Finkbeiner & Davis 1998. What follows is a detailed step-by-step guide to our systematic analysis: We select one of the aforementioned maps and locate the pixels where the value of the systematic is below the percentile level t. We compute the moments of the density contrast distribution in these pixels and their respective errors using bootstrapping. We
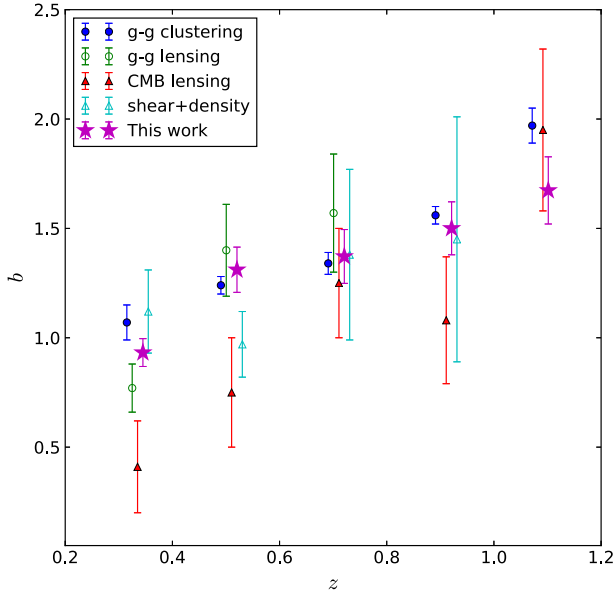
Figure 10. Bias obtained from second-order CiC, including systematic uncertainties from Section 6, compared with the two-point correlation study (Crocce et al. 2016), the CMB–galaxy cross-correlation study (Giannantonio et al. 2016), galaxy–galaxy lensing (Prat et al. 2018), and the shear + density analysis (Chang et al. 2016). The points for the same z have been separated in the horizontal axis for visualization purposes.

change the threshold to $t + 5$, repeat the process, and evaluate the difference between the moments calculated using this threshold divided by the moments in the original footprint $\Delta S_i(t)/\langle S_i \rangle$. An example of the results of this procedure can be found in Fig. 11. Note that the plot showing the variation of the moments with USNOB shows less points in the horizontal axis. Due to the discrete nature of the map of stellar counts, the 50th and 60th percentiles of the δ distribution of the stellar counts are the same; in order to avoid these problems, we make less bins in this case.

We consider that a systematic effect is present if the average of $\Delta S_i(t)/\langle S_i \rangle$ is different from zero at a 2σ confidence level or above for the different values of t from the 50th percentile to the 100th percentile. Then, we assign a systematic uncertainty equal to the value of this average. To be conservative, we consider these effects as independent, so we add them in quadrature. We summarize the main systematic effects observed in each redshift bin of our sample.

(i) Bin $0.2 < z < 0.4$:

(a) Seeing in i band: We assign a 3 per cent systematic uncertainty in S_4.
(b) Seeing in z band: We assign a 2.5 per cent systematic uncertainty in S_4.
(c) Sky brightness r band: We assign a 1 per cent systematic uncertainty in S_4.
(d) Sky brightness i band: We assign a 1 per cent systematic uncertainty in S_4.
(e) Airmass in g band: We assign a 1 per cent uncertainty in S_4.
(f) Airmass in r band: We assign a 1 per cent uncertainty in S_4.
(g) Airmass in i band: We assign a 1 per cent uncertainty in S_4.
(h) USNO-B stars: We assign a 4 per cent uncertainty to S_2, 7 per cent uncertainty to S_3, and 9 per cent to S_4.

(ii) Bin $0.4 < z < 0.6$:

(a) Seeing in z band: We assign a 1.5 per cent uncertainty to S_4.
(b) USNO-B stars: We assign a 4 per cent uncertainty to S_2, 3 per cent uncertainty to S_3, and 4 per cent uncertainty to S_4.

(iii) Bin $0.6 < z < 0.8$:

(a) Seeing in g band: We assign a 2 per cent uncertainty to S_4.
(b) Seeing in r band: We assign a 2 per cent uncertainty to S_4.
(c) Sky brightness i band: We assign a 1.5 per cent uncertainty to S_3 and 3 per cent systematic uncertainty to S_4.
(d) Airmass in g band: We assign a 2.5 per cent uncertainty to S_4.
(e) Airmass in r band: We assign a 2 per cent uncertainty to S_4.
(f) Airmass in z band: We assign a 1.5 per cent uncertainty to S_3 and 3 per cent uncertainty to S_4.
(g) USNO-B stars: We assign a 3 per cent uncertainty to S_3 and 5 per cent uncertainty to S_4.

(iv) Bin $0.8 < z < 1.0$:

(a) Seeing in g band: We assign a 2 per cent uncertainty to S_4.
(b) Sky brightness in i band: We assign a 2 per cent uncertainty to S_3 and a 3.5 per cent uncertainty to S_4.
(c) Airmass in g band: We assign a 2 per cent uncertainty to S_4.
(d) Airmass in r band: We assign a 3 per cent uncertainty to S_4.
(e) USNO-B stars: We assign a 3 per cent uncertainty to S_4.

(v) Bin $1.0 < z < 1.2$:

(a) The measurement of S_4 in this bin is dominated by systematics.
(b) Sky brightness in i band: We assign 2 per cent to S_3.
(c) Sky brightness z band: We assign 3 per cent to S_3.
(d) USNO-B stars: We assign a 4.5 per cent uncertainty to S_3.

The estimated systematic errors for the bias are propagated from the estimation of the systematics in S_2, S_3, and S_4. Their behaviour is compatible with the systematics found in Crocce et al. (2016). We use the same data masking, excluding regions with large systematic values to recover $w(\theta)$. The linear bias is more robust using CiC since the variance, S_2, is less affected by the small-scale power induced by the systematics given that these scales are smoothed out. On the other hand, the non-linear bias is more sensitive to the presence of systematics because they can induce asymmetries in the density contrast distribution.

6.1 Photometric redshift

Photometric redshift is one of the main potential sources of systematic effects in photometric surveys like DES. We have repeated the analysis in DES SV data for a second estimate of the photometric redshift using BPZ (Benitez 2000). In Fig. 12 we compare the results for the two photometric redshift codes and we see that they are in good agreement. The linear bias seems to be the most affected by the choice of a photometric redshift estimator but the results do not show any potential systematic biases. For the non-linear bias we get remarkably consistent results, showing the robustness of this method.
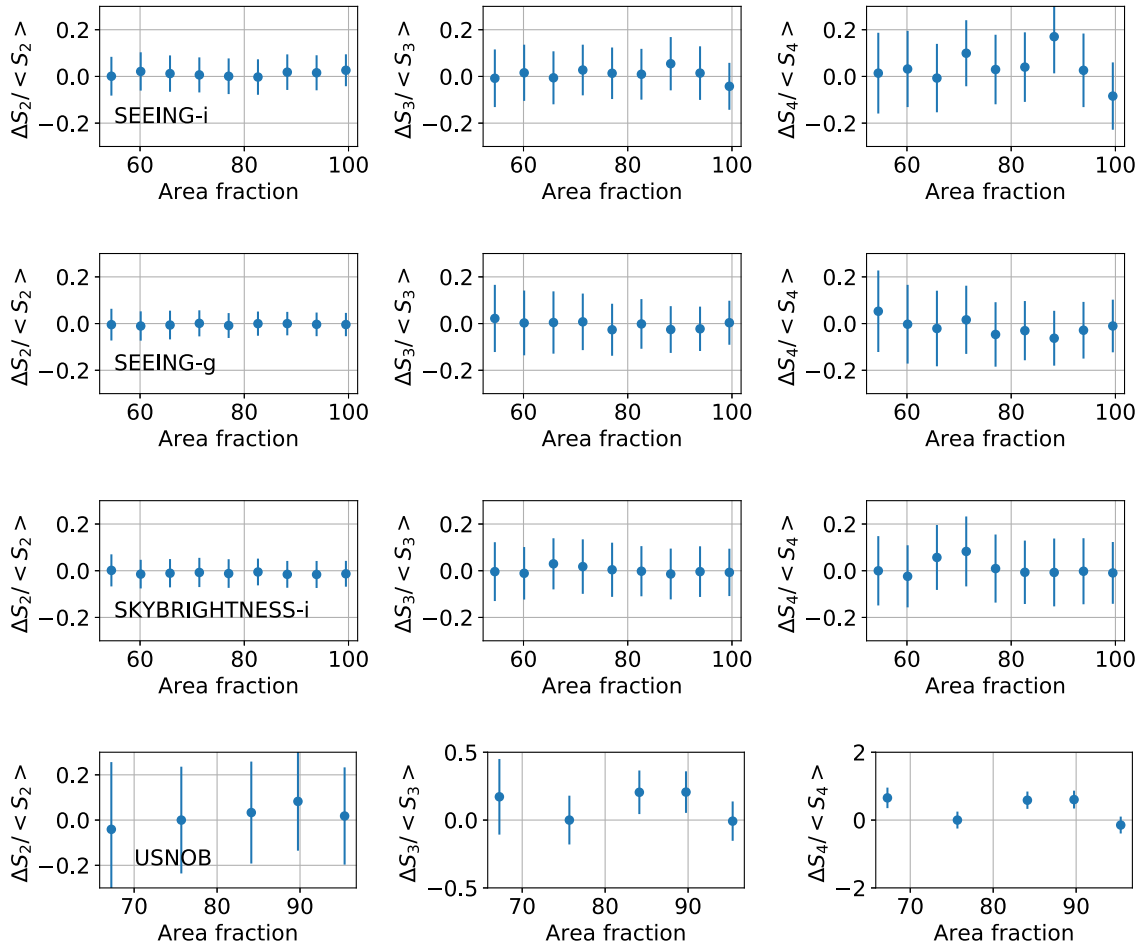
Figure 11. Dependence of the moments S_i with the variation in the value of potential systematic effects. We show an example for $N_{side} = 2048$ in the redshift bin $0.2 < z < 0.4$ using TPZ. The left column shows the behaviour for S_2, the middle column shows S_3, and the last column shows the results for S_4. The first row corresponds to the results for the seeing in the i band, the second row shows the results for the seeing in the g band, the third row shows the sky brightness in the i band. Finally the last row shows the evolution of the moments with the variation in the number of stars per pixel.

6.2 Biasing models

Apart from the terms that we considered in our model, Bel et al. (2015) found that non-local bias terms are responsible for the over-estimation of the linear bias from the three-point correlation in Pollack, Smith & Porciani (2014), Hoffmann et al. (2015), and Manera & Gaztañaga (2011) but that they should not significantly affect second-order statistics. As we mentioned previously in Section 5, we do not expect these terms to have a significant impact on our estimations because we analyse projected quantities over considerable volumes (note that we integrate in the cell and in the redshift slice). Having said that, we test the local and non-local models and find the results depicted in Fig. 13. We can see, as in the case of the simulation, that both models are consistent within errors. This means that choosing the local model does not introduce any systematic uncertainties in our linear bias measurements. However, it affects the b_2 measurements and their uncertainty since the new parameters introduced with these more complicated models are correlated with them. We check the probability of b_2 being zero for the different models and obtain the results in Table 1. We find b_2 to be different from zero at a 3σ level in the worst case (non-local). We also can see that in the first bin, none of the models fit the data well, which is not surprising, given that the range of (comoving) scales is very small ($\sim 1{-}20\,h^{-1}$ Mpc) and non-linear clustering dominates.

Finally, we are not considering stochastic models and we are assuming a Poisson shot-noise. This means that our measured b_2 could be entangled with stochasticity (Pen 1998; Sato & Matsubara 2013). We leave the study of stochasticity to future works.

6.3 Value of σ_8

As mentioned in previous sections, our bias estimation depends linearly on the value of σ_8. Thus, if the actual value of σ_8 is different from our assumed fiducial value, our results will be biased, and we have to correct for the difference using equation 11. This is why we introduce a systematic uncertainty of 1.4 per cent (the uncertainty level in σ_8 from Ade et al. 2014) which we add in quadrature to the statistical errors in the final estimation of the bias.

7 CONCLUSIONS

CiC is a simple but effective method to obtain the linear and non-linear bias. A good measurement of the galaxy bias is essential to maximize the performance of photometric redshift surveys because it can introduce a systematic effect on the determination of cosmological parameters. The galaxy bias is highly degenerate with other cosmological parameters and an independent method to determine
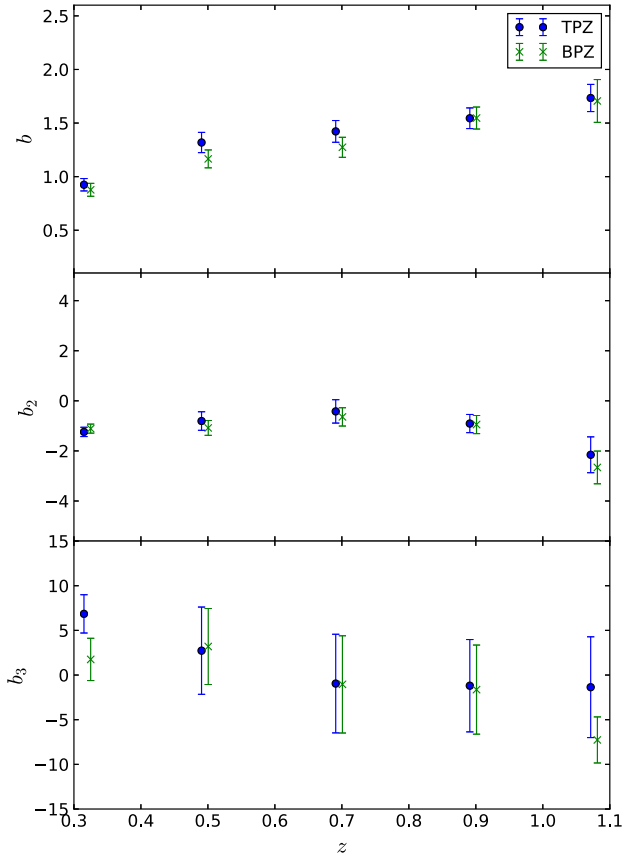
Figure 12. Bias obtained in the SV data from second-order CiC for TPZ (solid blue circles) and BPZ (green crosses). The results for a given redshift z have been separated in the figure for visualization purposes.
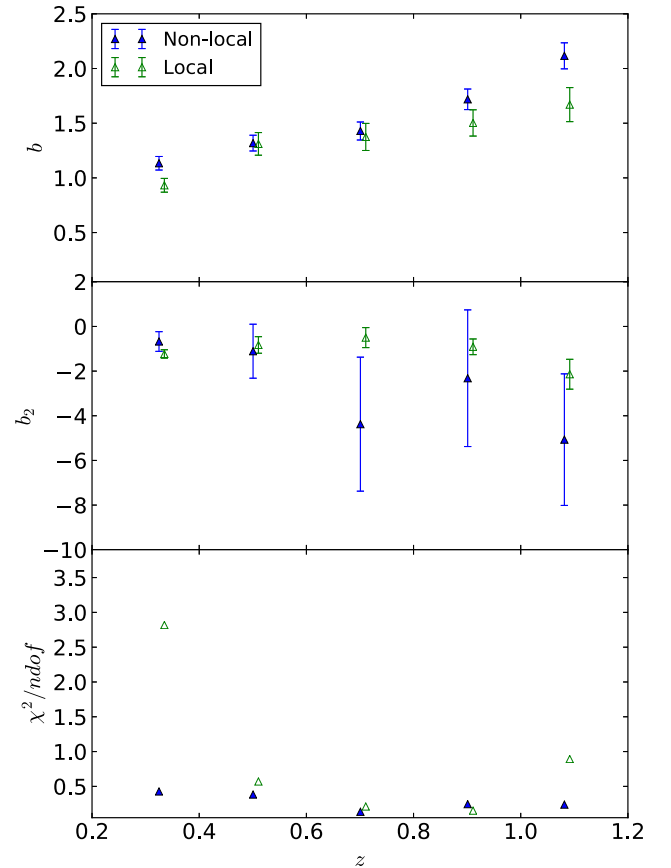

Figure 13. (Top) Comparison between the linear bias results obtained with CiC for SV using different biasing models: non-local (solid triangles) and local (open triangles) using the TPZ sample. (Middle) Comparison between b_2 results for the same models as above. (Bottom) Total reduced chi-square for each of the models.

Table 1. Comparison of the null hypothesis for b_2 in DES SV data for the different bias models considered in this work.

Bias model	χ^2	p-value	ndof
Local	64.75	3×10^{-13}	4
Non-local	12.63	0.013	4

it can break these degeneracies and improve the overall sensitivity to the underlying cosmology. In this paper we have developed a method to extract the bias from CiC. We use the MICE simulation to test our method and then perform measurements on the public Science Verification data from the Dark Energy Survey. The strength of this method is that it is based on a simple observable, the galaxy number counts, and is not demanding computationally.

We check that our linear bias measurement from CiC agrees with the real bias in the MICE simulation. Fig. 7 shows an agreement between our measurement and the one obtained using the angular two-point correlation function. We then obtain the linear bias in the SV data and find that it is in agreement with previous bias measurements from other DES analyses. In Fig. 10, we see that the CiC values are compatible with the two-point correlation study (Crocce et al. 2016), the CMB–galaxy cross-correlation study (Giannantonio et al. 2016), and the galaxy–galaxy lensing (Prat et al. 2018), and we demonstrate that these results are robust to the addition of new parameters in the biasing model, such as the non-local bias. Finally, we compute the non-linear bias parameters up to third order. We detect a significant non-zero b_2 component. It appears that the 2D and 3D predictions of the non-linear bias are in better agreement at larger scales, as expected. However, given the uncertainties associated with these quantities, it is difficult to draw any conclusions from b_3 despite its compatibility with the expected 3D prediction. When more data is available, we plan to check if we can improve our constraints on b_3 and whether the agreement with the 3D prediction improves as well. The systematic errors are in general lower than

the statistical errors, in agreement with the systematic study done by Crocce et al. (2016).

REFERENCES

Ade P. A. R. et al., 2014, A&A, 571, A16
Amiaux J., Scaramella R., Mellier, 2012, Clampin M. C., Giovanni F. G., MacEwen H. A., Oschmann J. M. Jr., in Proc. SPIE Conf. Ser. Vol. 8442, Space Telescopes and Instrumentation 2012: Optical, Infrared, and Millimeter Wave. SPIE, Bellingham, p. 84420Z
Bardeen J., Bond J., Kaiser N., Szalay A., 1986, ApJ, 304, 15
Bel J., Hoffmann K., Gaztañaga E., 2015, MNRAS, 453, 259
Benitez N., 2000, ApJ, 536, 571
Bernardeau F., 1994, ApJ, 433, 1
Bernardeau F., 1996, A&A, 312, 11
Bertin E., Arnouts S., 1996, A&AS, 117, 393
Blanton M., Cen R., Ostriker J. P., Strauss M. A., Tegmark M., 2000, ApJ, 531, 1
Bouchet F. R., Juszkiewicz R., Colombi S., Pellat R., 1992, ApJ, 394, L5
Carrasco Kind M., Brunner R. J., 2013, MNRAS, 432, 1483
Chang C. et al., 2016, MNRAS, 459, 3203
Clerkin L., et al., 2017, MNRAS, 466, 1444
Crocce M., Fosalba P., Castander F. J., Gaztañaga E., 2010, MNRAS, 403, 1353
Crocce M., Castander F. J., Gaztañaga E., Fosalba P., Carretero J., 2015, MNRAS, 453, 1513
Crocce M. et al., 2016, MNRAS, 455, 4301
Dark Energy Survey Collaboration, 2016, MNRAS, 460, 1270
Davis M., Geller M. J., Huchra J., 1978, ApJ, 221, 1
Dressler A., 1980, ApJ, 236, 351
Drlica-Wagner A. et al., 2018, ApJS, 235, 33
Efron B., 1979, Ann. Stat., 7, 1
Efstathiou G., Kaiser N., Saunders W., Lawrence A., Rowan-Robinson M., Ellis R. S., Frenk C. S., 1990, MNRAS, 247, 10P
Eriksen M., Gaztanaga E., 2015, MNRAS, 451, 1553
Foreman-Mackey D., Hogg D. W., Lang D., Goodman J., 2013, PASP, 125, 306
Fosalba P., Gaztañaga E., Castander F. J., Manera M., 2008, MNRAS, 391, 435
Frieman J. A., Gaztañaga E., 1999, ApJ, 521, L83
Fry J. N., 1996, ApJ, 461, L65
Fry J. N., Gaztañaga E., 1993, ApJ, 413, 447
Garcia-Fernandez M. et al., 2018, MNRAS, 476, 1071
Gaztañaga E., 1994, MNRAS, 268, 913
Gaztañaga E., Eriksen M., Crocce M., Castander F., Fosalba P. et al., 2012, MNRAS, 422, 2904
Giannantonio T. et al., 2016, MNRAS, 456, 3213
Gil-Marín H., Noreña J., Verde L., Percival W. J., Wagner C., Manera M., Schneider D. P., 2015, MNRAS, 451, 539
Górski K. M., Hivon E., Banday A. J., Wandelt B. D., Hansen F. K., Reinecke M., Bartelmann M., 2005, ApJ, 622, 759
Gruen D. et al., 2018, Phys. Rev. D., 98, 2, 23507
Heath D. J., 1977, MNRAS, 179, 351
Hoffmann K., Bel J., Gaztanaga E., 2015, MNRAS, 450, 1674
Ivezić Ž. et al., 2008, preprint (arXiv: 0805.2366)
Ivezić Ž., Connolly A., Vanderplas J., Gray A., 2014, Statistics, Data Mining and Machine Learning in Astronomy. Princeton Univ. Press, Princeton, NJ
Kaiser N., 1984, ApJ, 284, L9
Kollmeier J. A., Zasowski G., Rix, 2017, preprint (arXiv:1711.03234)
Le Fèvre O. et al., 2013, A&A, 559, A14
Leicht O., Uhlemann C., Villaescusa-Navarro F., Codis S., Hernquist L., Genel S., 2018, preprint (arXiv:1808.09968)
Leistedt B. et al., 2016, ApJS, 226, 24
Lilly S. J. et al., 2007, ApJS, 172, 70
Lilly S. J. et al., 2009, ApJS, 184, 218

Manera M., Gaztañaga E., 2011, MNRAS, 415, 383

Manera M., Sheth R. K., Scoccimarro R., 2010, MNRAS, 402, 589

Masci F. J., SWIRE Team, 2006, in Armus L., Reach W. T., eds, ASP Conf. Ser. Vol. 357, Large Scale Structure at 24 Microns in the SWIRE Survey. Astron. Soc. Pac., San Francisco, p. 271

Monet D. et al., 2003, ApJ, 125, 984

Mo H. J., White S. D. M., 1996, MNRAS, 282, 347

Norberg P., Baugh C., Hawkins E., Maddox S., 2002, MNRAS, 332, 827

Norberg P., Baugh C. M., Gaztañaga E., Croton D. J., 2009, MNRAS, 396, 19

Nusser A., Davis M., 1994, ApJ, 421, L1

Peebles P. J. E., 1980, The Large-Scale Structure of the Universe. Princeton Univ. Press, Princeton, NJ

Pen U.-L., 1998, ApJ, 504, 601

Pollack J. E., Smith R. E., Porciani C., 2014, MNRAS, 440, 555

Prat J. et al., 2018, MNRAS, 473, 1667

Press W. H., Schechter P., 1974, ApJ, 187, 425

Pujol A., Hoffmann K., Jiménez N., Gaztañaga E., 2017, A&A, 598, A103

Ross A. J., Brunner R. J., Myers A. D., 2006, ApJ, 649, 48

Rozo E. et al., 2016, MNRAS, 461, 1431

Sánchez E. et al., 2011, MNRAS, 411, 277

Sánchez C. et al., 2014, MNRAS, 445, 1482

Sato M., Matsubara T., 2013, Phys. Rev. D, 87, 123523

Scherrer R. J., Weinberg D. H., 1998, ApJ, 504, 607

Schlegel D., Finkbeiner D., Davis M., 1998, ApJ, 500, 525

Sheth R. K., Tormen G., 1999, MNRAS, 308, 119

Szapudi I., 1998, ApJ, 497, 16

Szapudi I. et al., 2002, ApJ, 570, 75

Tegmark M., Peebles P. J. E., 1998, ApJ, 500, L79

Willmer C. N. A., Maia M. A. G., Mendes S. O., Alonso M. V., Rios L. A., Chaves O. L., de Mello D. F., 1999, AJ, 118, 1131

Wolk M., McCracken H. J., Colombi S., Fry J. N., Kilbinger M., Hudelot P., Mellier Y., Ilbert O., 2013, MNRAS, 435, 2

Yang A., Saslaw W. C., 2011, ApJ, 729, 123

Zehavi I., Blanton M., Frieman J., Weinberg D., 2002, ApJ, 571, 172

APPENDIX A: DIFFERENT PIXEL SHAPES

We check with the MICE simulation in a thin redshift bin ($0.95 < z < 1.05$) that as long as we have regular polygon pixels the difference in the moments of the density contrast is negligible. In Fig. A1 we see that the difference is negligible for the more symmetrical pixels and higher for less symmetrical ones. The angular aperture, θ, is estimated as the square root of the pixel area. We compare rectangular pixels with HEALpix pixels. We divide the sphere into rectangular pixels taking n_{ra} parts in right ascension and n_{ct} parts in sin dec where the number of pixels is npix $= n_{ra} \times n_{ct} = 12(N_{side} \times N_{side})$. We have taken six different pixel shapes numbered from 1 to 6. Pixels number 3 ($n_{ra} = 3N_{side}, n_{ct} = 4N_{side}$), 4 ($n_{ra} = 4N_{side}, n_{ct} = 3N_{side}$), and 6 ($n_{ra} = 6N_{side}, n_{ct} = 2N_{side}$) are close to being squares, but pixels number 1 ($n_{ra} = 12N_{side}, n_{ct} = 1N_{side}$), 2 ($n_{ra} = 1N_{side}, n_{ct} = 12N_{side}$), and 5 ($n_{ra} = 2N_{side}, n_{ct} = 6N_{side}$) are far from being regular polygons. When we compare square and HEALpix pixels, we see that the measured moments are in perfect agreement.
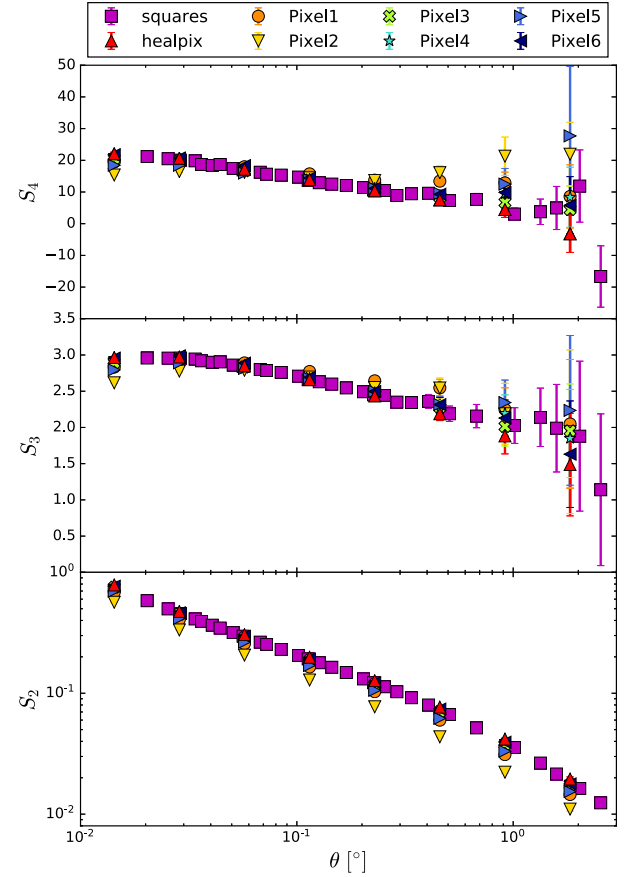

Figure A1. Moments of the density contrast distribution as a function of the cell scale using data from MICE in the redshift slice $0.95 < z < 1.05$ for different pixel shapes. Pixels number 3 ($n_{ra} = 3N_{side}, n_{ct} = 4N_{side}$), 4 ($n_{ra} = 4N_{side}, n_{ct} = 3N_{side}$), and 6 ($n_{ra} = 6N_{side}, n_{ct} = 2N_{side}$) are close to being squares, but pixels number 1 ($n_{ra} = 12N_{side}, n_{ct} = 1N_{side}$), 2 ($n_{ra} = 1N_{side}, n_{ct} = 12N_{side}$), and 5 ($n_{ra} = 2N_{side}, n_{ct} = 6N_{side}$) are far from being regular polygons.

APPENDIX B: BOUNDARY EFFECTS

To deal with the boundary effects of an irregularly shaped area, we use the mask and degrade its resolution to match each of the pixel scales being used. However, degrading the mask (or increasing the scale) results in an increasing number of partially filled pixels. Only a fraction $r_A = A_{filled}/A_{pixel}$ remain completely inside the footprint. This means that if we assign the same scale to all the pixels of a given N_{side} value, some pixels will be effectively mapping a different scale. To solve this problem we can either require a minimum fraction of the pixel to be full, $r_A \geq X$, or compute the fraction of full pixels and
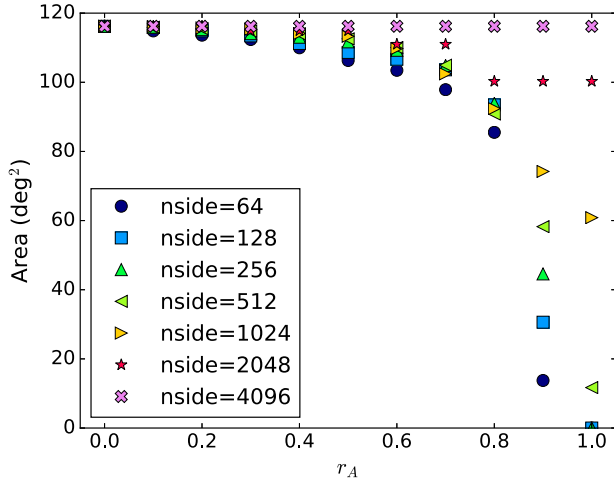
Figure B1. Area covered by different `HEALpix` pixellation resolutions as a function of the minimum fraction of pixel coverage of said resolution with respect to the $N_{side} = 4096$ footprint (larger pixels from lower N_{side} will be partially filled at times). This test is done using the MICE simulation considering the same footprint as the SV data set.
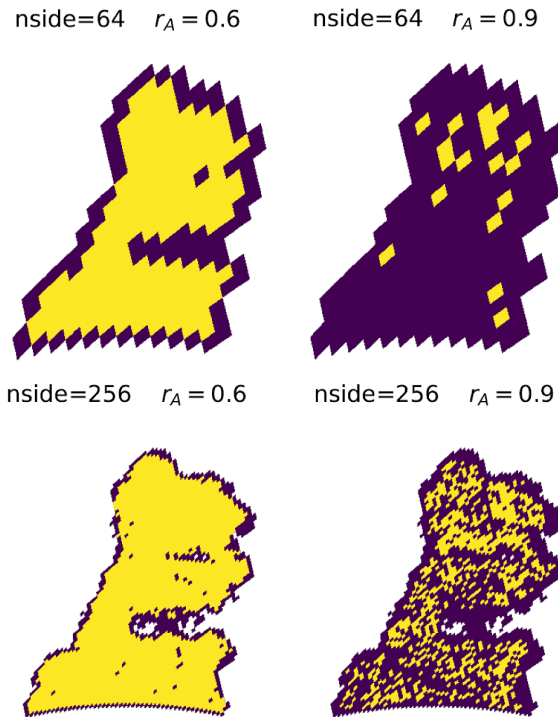

Figure B2. DES SV mask for different N_{side} (64, 256) and different area cuts $r_A = 0.6, 0.9$. The pixels that we discard are blue and the ones that we keep are red. The bigger the pixel, the larger the amount of data we lose.

perform CiC for that scale. We prefer to use the former because we consider that the scales where we perform the study appropriately map the variations of the density field in which we are interested. This approach also helps to avoid certain boundary effects. For small pixel sizes (similar to the size in the mask), given the large number of pixels, we can safely choose $r_A = 1$. For bigger pixels we try to find a compromise between the amount of area that we lose and the boundary effects. In Figs B1 and B2 we show the area loss using data from MICE in the redshift bin $0.95 < z < 1.05$
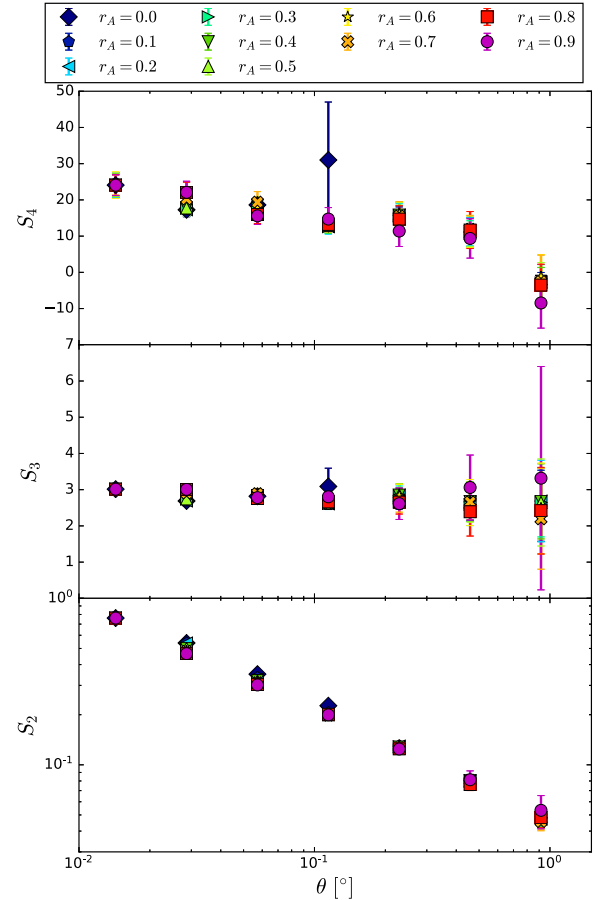

Figure B3. Moments of the density contrast distribution obtained from MICE ($0.95 < z < 1.05$) considering the same footprint as the SV data for different values of the fraction of the pixel inside the mask, r_A. The results for a given scale θ have been separated in the figure for visualization purposes.

with the SV mask for different thresholds in r_A and in Fig. B3 the change in the moments for these different area cuts. We see that if we choose pixels that are completely contained inside the mask ($r_A = 1.0$), we lose a lot of area for smaller values of N_{side}; however, very little area is lost for large values of N_{side}. It can be seen that results are consistent for the different threshold values for r_A. We also see that if we take all the pixels ($r_A \geq 0$), the difference in the moments is considerable in some cases, and we cannot take just all the pixels inside the mask ($r_A = 1$) because we run out of them for large scales. We set a threshold $r_A \geq 0.9$ to ensure that the pixels are almost completely embedded in the footprint. This prevents us from mixing scales even for the largest pixel sizes. This can be noted in Fig. B1 where a large drop in area occurs between $r_A = 0.8$ and $r_A = 0.9$ for $N_{side} \leq 1024$, setting this threshold naturally. For most scales this threshold does not change the errors. By choosing $r_A \geq 0.9$ the effective cell sizes are well determined and the errors are reasonably small.

APPENDIX C: SIMULTANEOUS FITS RESULTS

In this section we show the fitting results for the simultaneous fits in MICE. In Figs C1 and C2, the red line corresponds to the mean value of the samples and the grey lines are the different models evaluated by the MCMC.
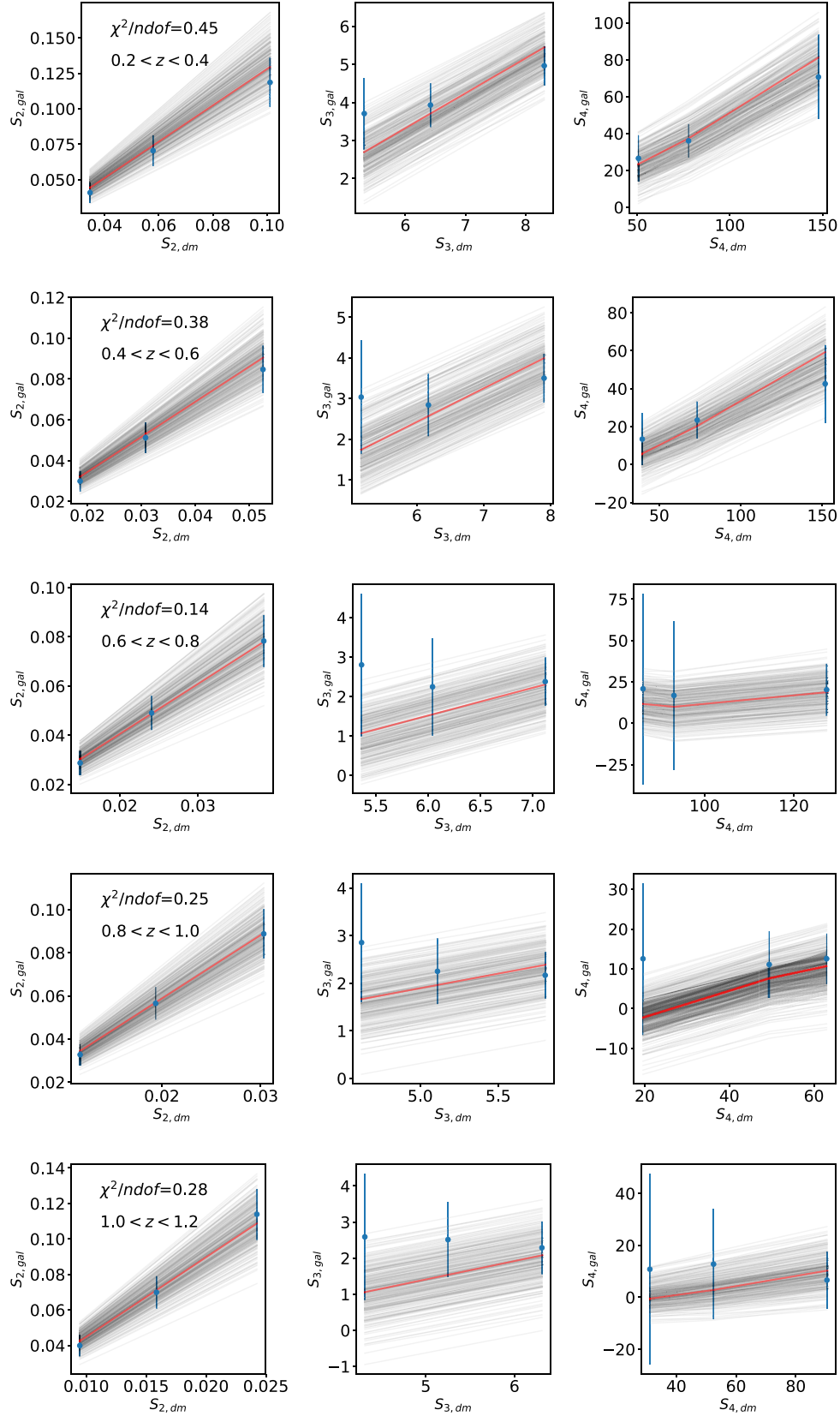
Figure C1. Fit results for the non-linear bias simultaneous fits method using MICE with Gaussian photo-z. The points are the measured moments and the error bars are calculated by adding in quadrature the uncertainties from the moments in the dark matter and the galaxies. The thick dark line is the best-fitting curve corresponding to the mean of the posterior distribution. The thin grey lines are the different models evaluated by the MCMC. The top row corresponds to the first redshift bin ($0.2 < z < 0.4$), the second row corresponds to the second redshift bin, and so on.
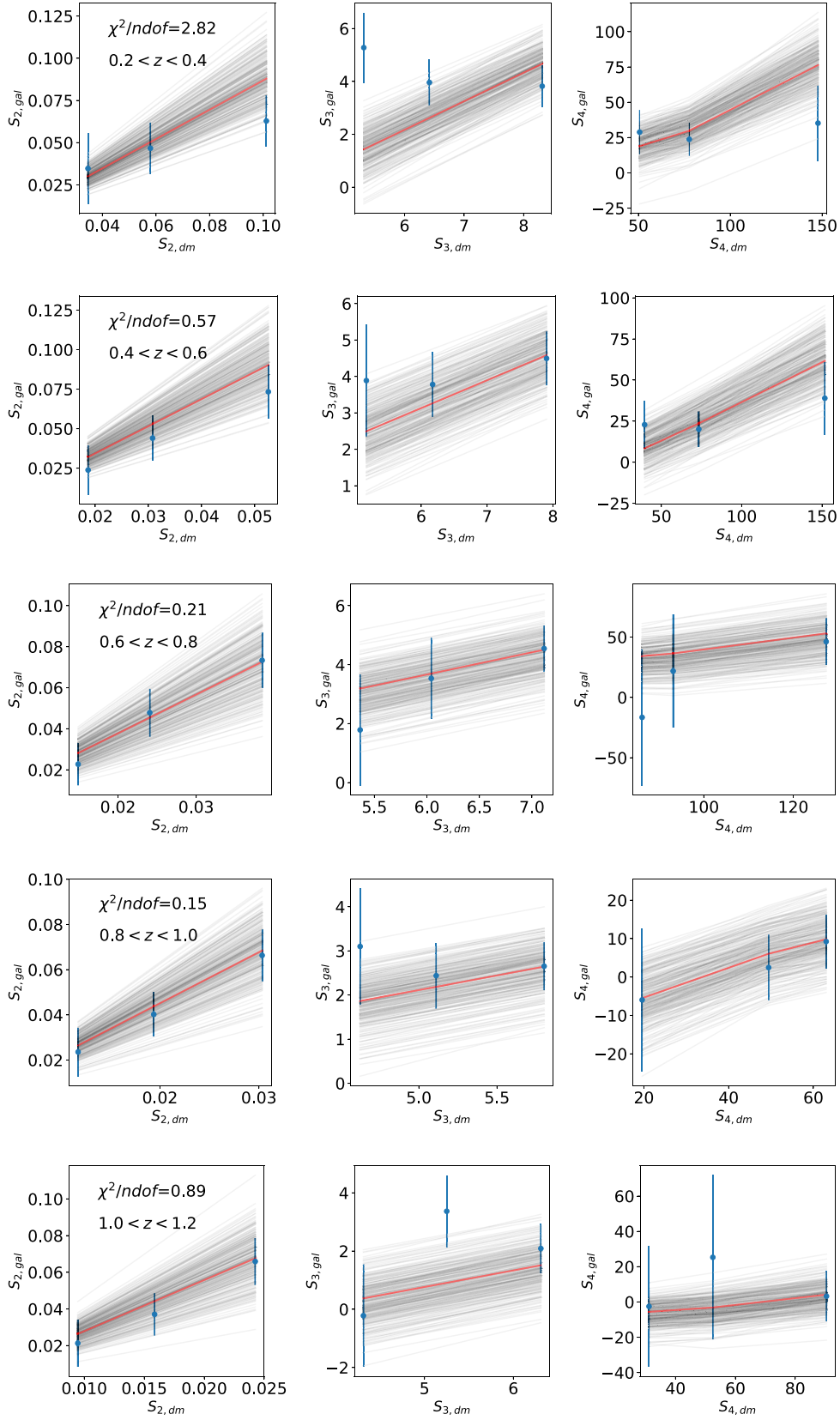
Figure C2. Non-linear bias fits for DES SV data. See caption in Fig. C1 for more details.

[1]*Instituto de Fisica Teorica UAM/CSIC, Universidad Autonoma de Madrid, E-28049 Madrid, Spain*

[2]*Department of Physics and Astronomy, University of California, Irvine 92602, USA*

[3]*Centro de Investigaciones Energéticas, Medioambientales y Tecnológicas (CIEMAT), E-28040 Madrid, Spain*

[4]*Department of Physics and Astronomy, University of California, Riverside 92521, USA*

[5]*Kavli Institute for Cosmological Physics, University of Chicago, Chicago, IL 60637, USA*

[6]*DEDIP/DAP, IRFU, CEA, Université Paris-Saclay, F-91191 Gif-sur-Yvette, France*

[7]*Université Paris Diderot, AIM, Sorbonne Paris Cité, CEA, CNRS, F-91191 Gif-sur-Yvette, France*

[8]*Fermi National Accelerator Laboratory, PO Box 500, Batavia, IL 60510, USA*

[9]*Institut d'Estudis Espacials de Catalunya (IEEC), E-08193 Barcelona, Spain*

[10]*Institute of Space Sciences (ICE, CSIC), Campus UAB, Carrer de Can Magrans, s/n, E-08193 Barcelona, Spain*

[11]*Center for Cosmology and AstroParticle Physics, Department of Physics, the Ohio State University, 191 W Woodruff Ave,Columbus, OH 43210, USA*

[12]*Cerro Tololo Inter-American Observatory, National Optical Astronomy Observatory, Casilla 603, La Serena, Chile*

[13]*Institute of Cosmology & Gravitation, University of Portsmouth, Portsmouth PO1 3FX, UK*

[14]*CNRS, UMR 7095, Institut d'Astrophysique de Paris, F-75014 Paris, France*

[15]*Sorbonne Universités, UPMC Univ Paris 06, UMR 7095, Institut d'Astrophysique de Paris, F-75014 Paris, France*

[16]*Department of Physics & Astronomy, University College London, Gower Street, London WC1E 6BT, UK*

[17]*Kavli Institute for Particle Astrophysics & Cosmology, PO Box 2450, Stanford University, Stanford, CA 94305, USA*

[18]*SLAC National Accelerator Laboratory, Menlo Park, CA 94025, USA*

[19]*Laboratório Interinstitucional de e-Astronomia - LIneA, Rua Gal. José Cristino 77, Rio de Janeiro, RJ-20921-400, Brazil*

[20]*Observatório Nacional, Rua Gal. José Cristino 77, Rio de Janeiro, RJ-20921-400, Brazil*

[21]*Department of Astronomy, University of Illinois at Urbana-Champaign, 1002 W. Green Street, Urbana, IL 61801, USA*

[22]*National Center for Supercomputing Applications, 1205 West Clark St., Urbana, IL 61801, USA*

[23]*Institut de Física d'Altes Energies (IFAE), the Barcelona Institute of Science and Technology, Campus UAB, E-08193 Bellaterra (Barcelona), Spain*

[24]*Department of Astronomy, University of Michigan, Ann Arbor, MI 48109, USA*

[25]*Department of Physics, University of Michigan, Ann Arbor, MI 48109, USA*

[26]*Department of Physics, ETH Zurich, Wolfgang-Pauli-Strasse 16, CH-8093 Zurich, Switzerland*

[27]*Santa Cruz Institute for Particle Physics, Santa Cruz, CA 95064, USA*

[28]*Harvard-Smithsonian Center for Astrophysics, Cambridge, MA 02138, USA*

[29]*Australian Astronomical Observatory, North Ryde, NSW 2113, Australia*

[30]*Departamento de Física Matemática, Instituto de Física, Universidade de São Paulo, CP 66318, São Paulo, SP 05314-970, Brazil*

[31]*Department of Physics and Astronomy, University of Pennsylvania, Philadelphia, PA 19104, USA*

[32]*George P. and Cynthia Woods Mitchell Institute for Fundamental Physics and Astronomy, and Department of Physics and Astronomy, Texas A&M University, College Station, TX 77843, USA*

[33]*Institució Catalana de Recerca i Estudis Avançats, E-08010 Barcelona, Spain*

[34]*Department of Physics and Astronomy, Pevensey Building, University of Sussex, Brighton BN1 9QH, UK*

[35]*School of Physics and Astronomy, University of Southampton, Southampton SO17 1BJ, UK*

[36]*Physics Department, Brandeis University, 415 South Street, Waltham, MA 02453, USA*

[37]*Instituto de Física Gleb Wataghin, Universidade Estadual de Campinas, 13083-859 Campinas, SP, Brazil*

[38]*Computer Science and Mathematics Division, Oak Ridge National Laboratory, Oak Ridge, TN 37831, USA*

[39]*Argonne National Laboratory, 9700 South Cass Avenue, Lemont, IL 60439, USA*

This paper has been typeset from a TEX/LATEX file prepared by the author.